



1 **Frazil ice growth and production during katabatic wind events in the Ross Sea, Antarctica**

2

3 Lisa De Pace¹, Madison Smith², Jim Thomson², Sharon Stammerjohn³, Steve Ackley⁴, and Brice
4 Loose⁵

5

6 ¹Department of Science, US Coast Guard Academy, New London CT

7 ²Applied Physics Laboratory, University of Washington, Seattle WA

8 ³Institute for Arctic and Alpine Research, University of Colorado at Boulder, Boulder CO

9 ⁴University of Texas at San Antonio, San Antonio TX

10 ⁵Graduate School of Oceanography, University of Rhode Island, Narragansett RI

11

12 *Correspondence to:* Brice Loose (bloose@uri.edu)

13

14 ABSTRACT: During katabatic wind events in the Terra Nova Bay and Ross Sea polynyas, wind
15 speeds exceeded 20 m s^{-1} , air temperatures were below -25°C , and the mixed layer extended as
16 deep as 600 meters. Yet, upper ocean temperature and salinity profiles were not perfectly
17 homogeneous, as would be expected with vigorous convective heat loss. Instead, the profiles
18 revealed bulges of warm and salty water directly beneath the ocean surface and extending
19 downwards tens of meters. Considering both the colder air above and colder water below, we
20 suggest the increase in temperature and salinity reflects latent heat and salt release during
21 unconsolidated frazil ice production within the upper water column. We use a simplified salt
22 budget to analyze these anomalies to estimate in-situ frazil ice concentration between 332×10^{-3}
23 and $24.4 \times 10^{-3} \text{ kg m}^{-3}$. Contemporaneous estimates of vertical mixing by turbulent kinetic
24 energy dissipation reveal rapid convection in these unstable density profiles, and mixing
25 lifetimes from 2 to 12 minutes. The corresponding median rate of ice production is 26 cm day^{-1}
26 and compares well with previous empirical and model estimates. Our individual estimates of ice
27 production up to 378 cm day^{-1} reveal the intensity of short-term ice production events during the
28 windiest episodes of our occupation of Terra Nova Bay Polynya.

29



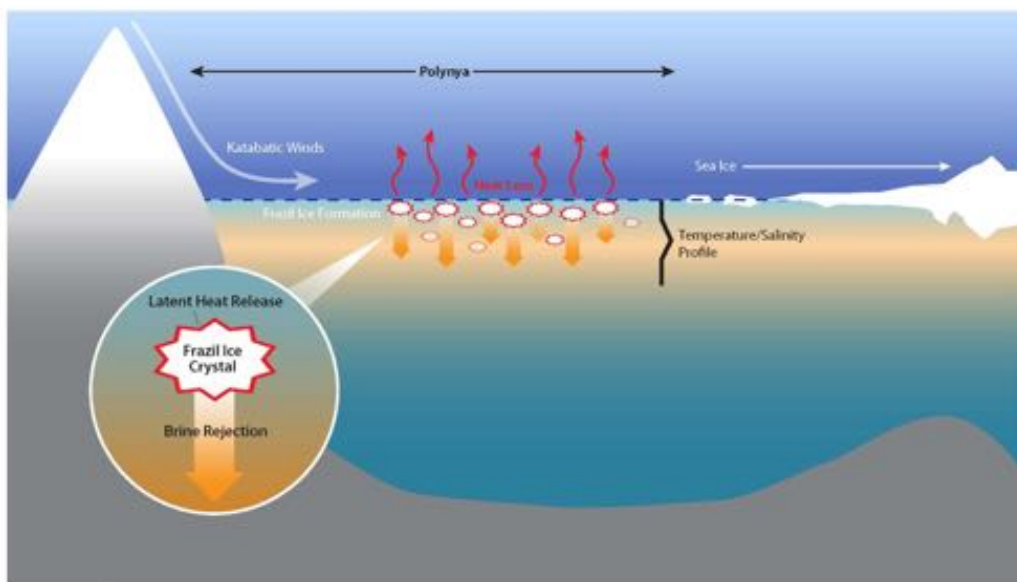
30 **1. INTRODUCTION**

31

32 Latent heat polynyas form in areas where prevailing winds or oceanic currents create
33 divergence in the ice cover, leading to openings either surrounded by extensive pack ice or
34 bounded by land on one side and pack ice on the other (coastal polynyas) (Armstrong, 1972;
35 Park et al, 2018). The open water of polynyas is critical for air-sea heat exchange, since ice
36 covered waters are one to two orders of magnitude better insulated (Fusco et al., 2009; Talley et
37 al, 2011). A key feature of coastal or latent heat polynyas are katabatic winds (Figure 1), which
38 originate as cold, dense air masses that form over the continental ice sheets of Antarctica. These
39 air masses flow as sinking gravity currents, descending off the glaciated continent, or in the case
40 of the Terra Nova Bay Polynya, through the Transantarctic mountain range. These flows are
41 often funneled and strengthened by mountain-valley topography. The katabatic winds create and
42 maintain latent heat polynyas. This research focuses on in-situ measurements taken from two
43 coastal latent heat polynyas in the Ross Sea, the Terra Nova Bay polynya and the Ross Sea
44 polynya.

45

46





47 Figure 1: Schematic of a latent heat or coastal polynya. The polynya is kept open from katabatic
48 winds which drive ice advection, oceanic heat loss and frazil ice formation. Ice formation results
49 in oceanic loss of latent heat to the atmosphere and brine rejection (Talley et al, 2011). Inset is a
50 schematic of Frazil ice formation that depicts the release of latent heat of fusion and brine
51 rejection as a frazil ice crystal is formed.

52

53 The extreme oceanic heat loss in polynyas can generate “supercooled” water, which is
54 colder than the eutectic freezing point (Skogseth et al., 2009; Dmitrenk et al, 2010; Matsumura
55 & Ohshima, 2015). Supercooled water is the precursor to ice nucleation and in-situ ice
56 production. The first type of sea ice to appear are found as fine disc-shaped or dendritic crystals
57 called frazil ice. These frazil ice crystals (Figure 1 inset) are about 1 to 4 millimeters in diameter
58 and 1-100 micrometers in thickness (Heorton & Feltham, 2017; Martin, 1981; Ushio &
59 Wakatsuchi, 1993; Wlichinsky et al., 2015). In polynyas, large net heat losses eventually lead to
60 frazil ice production where katabatic winds and cold air temperatures transport of ice crystals
61 away from the formation site near the ocean surface and into the water column. Both conditions
62 are achieved in polynyas by (Coachman, 1966). Katabatic winds sustain the polynya by clearing
63 frazil ice, forming pancake ice which piles up at the polynya edge to form a consolidated ice
64 cover (Morales Maqueda et al, 2004; Ushio and Wakatsuchi, 1993).

65 Brine rejection (Cox & Weeks, 1983) and latent heat release during ice production, can
66 lead to dense water formation. Over the Antarctic continental shelf, this process produces the
67 precursor to Antarctic Bottom Water (AABW), a water mass known as High Salinity Shelf Water
68 (HSSW) (Talley et al, 2011). In the case of the Ross Sea, the cold, dense HSSW formed on the
69 shelf eventually becomes AABW off the shelf, the densest water in global circulation (Cosimo &
70 Gordon, 1998; Jacobs, 2004; Martin, et al., 2007; Tamura et al.; 2007). Terra Nova Bay polynya
71 produces especially dense HSSW, and produces approximately 1-1.5 Sv of HSSW annually
72 (Buffoni et al., 2002; Orsi & Wiederwohl, 2009; Sansivero et al, 2017; Van Woert 1999a,b).

73 Given the importance of AABW to global thermohaline circulation, polynya ice
74 production rates have been widely studied and modeled. Gallee (1997), Petrelli et al. (2008),
75 Fusco et al. (2002), and Sansivero et al. (2017) used models to calculate polynya ice production



76 rates on the order of tens of centimeters per day. Schick (2018) and Kurtz and Bromwich (1985)
77 used heat fluxes to estimate polynya ice production rates, also on the order of tens of centimeters
78 per day. However, quantitative estimation of polynya ice production is challenging due to the
79 difficulty of obtaining direct measurements (Fusco et al., 2009; Tamura et al., 2007).

80

81 **1.2 Motivation for this article**

82 During a late autumn oceanographic expedition to the Ross Sea as part of the PIPERS (Polynyas,
83 Ice Production and seasonal Evolution in the Ross Sea) project we measured CTD profiles in the
84 Ross Sea coastal polynyas during katabatic wind events. Despite air temperatures that were well
85 below freezing and strong winds frequently in excess of the katabatic threshold, these CTD
86 profiles presented signatures of warmer water near the surface. The excess temperature was
87 accompanied by similar signatures of saltier water. During this period, we also observed long
88 wind rows of frazil ice. We hypothesized that the excess temperature was evidence of latent heat
89 of fusion from frazil ice formation, and that the excess salinity was evidence of brine rejection
90 from frazil ice formation. To test these hypotheses, we had to first evaluate the fidelity of these
91 CTD measurements by comparing the shape and size of the profile anomalies with estimates of
92 the CTD precision and stability, and by using supporting evidence of the atmospheric conditions
93 that are thought to drive frazil ice formation (e.g. temperature and wind speed). This analysis is
94 described below, followed by our estimates of frazil ice concentration using the temperature and
95 salinity anomalies (§4). To better understand the importance of frazil formation, we computed
96 the lifetime of these anomalies (§5), which in turn yielded frazil ice production rates (§6). Last,
97 we discuss the implications for spatial variability of ice production and application for further
98 polynya sea ice production estimates.

99

100

101 **2. STUDY AREA AND DATA**

102

103 **2.1 The Terra Nova Bay Polynya and Ross Sea Polynya**

104

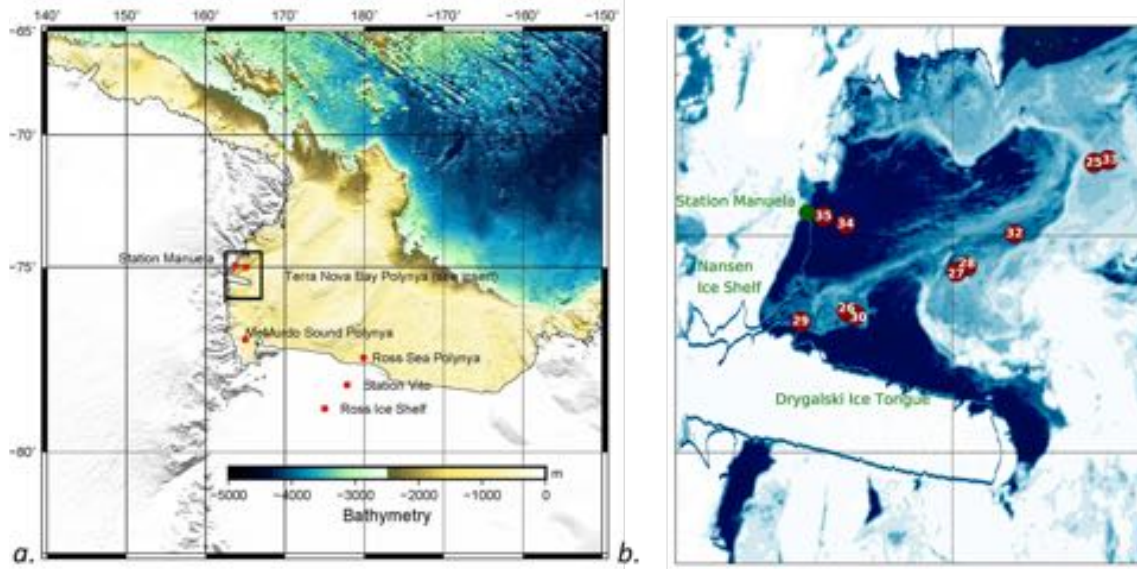


105 The Ross Sea, a southern extension of the Pacific Ocean, abuts Antarctica along the
106 Transantarctic Mountains and has three recurring latent heat polynyas: Ross Sea polynya (RSP),
107 Terra Nova Bay polynya (TNBP), and McMurdo Sound polynya (MSP) (Martin et al., 2007).
108 The RSP is Antarctica's largest recurring polynya, the average area of the RSP is 27,000 km² but
109 can grow as large as 50,000 km², depending on environmental conditions (Morales Maqueda, et
110 al., 2004; Park et al, 2018). It is located in the central and western Ross Sea to the east of Ross
111 Island, adjacent to the Ross Ice Shelf (Figure 2), and typically extends the entire length of the
112 Ross Ice Shelf (Martin et al., 2007; Morales Maqueda et al., 2004). TNBP is bounded to the
113 south by the Drygalski ice tongue, which serves to control the polynya maximum size (Petrelli et
114 al., 2008). TNBP and MSP, the smallest of the three polynyas, are both located in the western
115 Ross Sea (Figure 2) (Petrelli et a;., 2008). The area of TNBP, on average is 1300 km², but can
116 extend up to 5000 km²; the oscillation period of TNBP broadening and contracting is 15-20 days
117 (Bromwich & Kurtz, 1984). This paper focuses primarily on TNBP and secondarily on RSP,
118 where our observations were taken.

119

120 During the autumn and winter season, Morales Maqueda et al., (2004) estimated TNBP
121 cumulative ice production to be around 40-60 meters of ice, or approximately 10% of the annual
122 sea ice production that occurs on the Ross Sea continental shelf. The RSP has a lower daily ice
123 production rate, but produces three to six times as much as TNBP annually due to its much larger
124 size (Petrelli et al., 2008).

125



126 Figure 2: Map of the Ross Sea and the Terra Nova Bay Polynya. a) Overview of the Ross Sea ,
127 Antarctica highlighting the locations of the three recurring polynyas: Ross Sea Polynya (RSP),
128 Terra Nova Bay Polynya (TNBP), and McMurdo Sound Polynya (MSP). Map highlights the
129 2014 General Bathymetric Chart of the Oceans one-degree grid. b) Terra Nova Bay Polynya
130 Insert as indicated by black box in panel a. MODIS image of TNBP with the 10 CTD stations
131 with anomalies shown. Not included is CTD Station 40, the one station with an anomaly located
132 in the RSP. (CTD Station 40 is represented on Figure 2a as the location of the Ross Sea
133 Polynya.) Date of MODIS image is March 13, 2017; MODIS from during cruise dates could not
134 be used due to the lack of daylight and high cloud cover.

135

136 2.2 PIPERS Expedition

137

138 We collected these data during late autumn, from April 11 to June 14, 2017 aboard the
139 RVIB Nathaniel B. Palmer (NB Palmer, NBP17-04). More information about the research
140 activities during the PIPERS expedition is available at
141 <http://www.utsa.edu/signl/pipers/index.html>. Vertical profiles of Conductivity, Temperature, and
142 Depth (CTD) were taken at 58 stations within the Ross Sea. For the purposes of this study, we



143 focus on the 13 stations (CTD 23-35) that occurred within the TNBP and 4 stations (CTD 37-40)
144 within the RSP during katabatic wind events (Figure 2). In total, 11 of these 17 polynya stations
145 will be selected for use in our analysis, as described in §3.1.

146

147 **2.3 CTD measurements**

148

149 The CTD profiles were carried out using a Seabird 911 CTD (SBE 911) attached to a 24
150 bottle CTD rosette, which is supported and maintained by the Antarctic Support Contract (ASC).
151 The SBE 911 was deployed from the starboard Baltic Room. Each CTD cast contains both down
152 and up cast profiles. In many instances, the upcast recorded a similar thermal and haline
153 anomaly. However the 24 bottle CTD rosette package creates a large wake that disturbs the
154 readings on the upcast, so only the down cast profiles are used.

155 The instrument resolution is important for this study, because the anomalous profiles
156 were identified by comparing the near surface CTD measurements with other values within the
157 same profiles. The reported initial accuracy for the SBE 911 is $\pm 0.0003 \text{ S m}^{-1}$, $\pm 0.001 \text{ }^{\circ}\text{C}$, and
158 0.015% of the full-scale range of pressure for conductivity, temperature, and depth respectively.
159 Independent of the accuracy stated above, the SBE 911 can resolve differences in conductivity,
160 temperature, and pressure on the order of 0.00004 S m^{-1} , $0.0002 \text{ }^{\circ}\text{C}$ and 0.001% of the full range,
161 respectively (SeaBird Scientific, 2018). The SBE 911 samples at 24 Hz with an e-folding time
162 response of 0.05 seconds for conductivity and temperature. The time response for pressure is
163 0.015 seconds.

164 The SBE 911 data were post-processed with post-calibrations by Seabird, following
165 standard protocol, and quality control parameters. Profiles were bin-averaged at two size
166 intervals: one-meter depth bins and 0.1-meter depth bins, to compare whether bin averaging
167 influenced the heat and salt budgets. Since we observed no difference between the budget
168 calculations derived from one-meter vs 0.1-meter bins, the results using one-meter bins are
169 presented in this publication. All thermodynamic properties of seawater were evaluated via the
170 Gibbs Seawater toolbox, which uses the International Thermodynamic Equation Of Seawater –
171 2010 (TEOS-10).



172

173

174 **2.4 Weather observations**

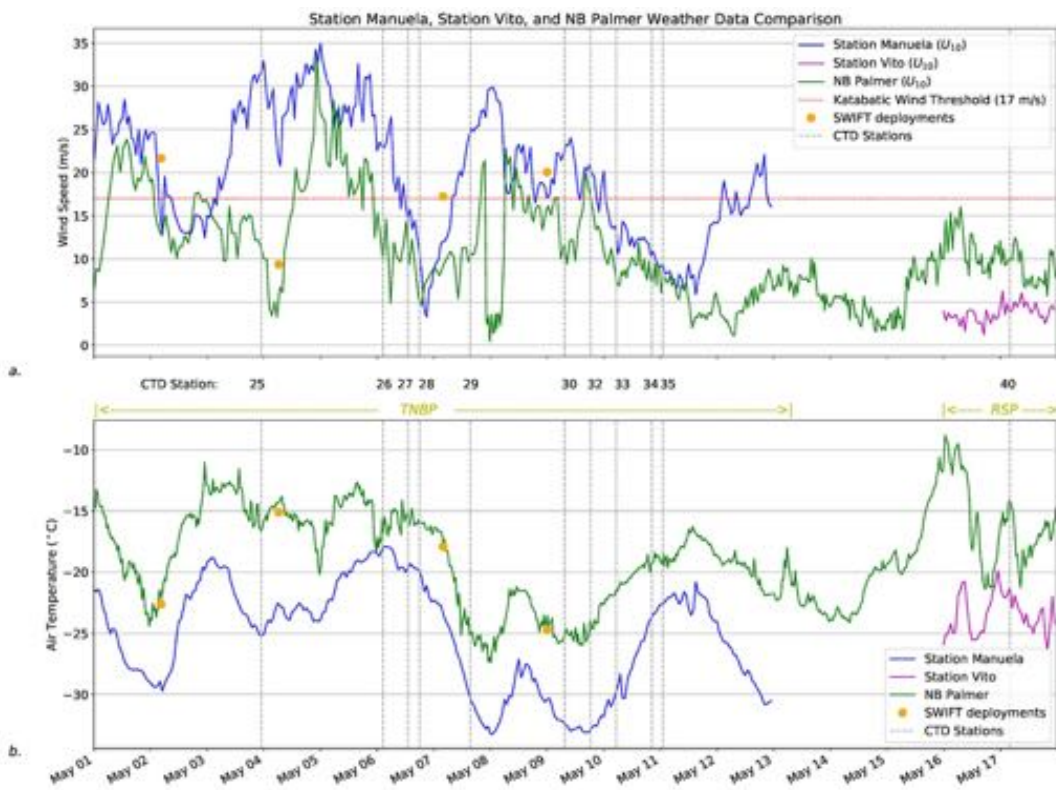
175 Multiple katabatic wind events were observed within the TNBP and RSP during the
176 PIPERS expedition. Weather observations from the NB Palmer meteorological suite during these
177 periods were compared with observations from automatic weather stations Manuela, on
178 Inexpressible Island, and Station Vito, on the Ross Ice Shelf (Figure 2a). Observations from all
179 three were normalized to a height of 10 meters (Figure 3). The NB Palmer was in TNB from
180 May 1 through May 13; during this period the hourly wind speed and air temperature data from
181 Weather Station Manuela follow the same pattern, with shipboard observations from the NB
182 Palmer observations being lower in intensity (lower wind speed, warmer temperatures) than
183 Station Manuela. In contrast, the wind speed and air temperature from NB Palmer during its
184 occupation in RSP (May 16-18) is compared to Station Vito. At Station Vito, the air temperature
185 is colder, but the wind speed is less intense. Whereas at Station Manuela (TNBP) the winds are
186 channelized and intensified through adjacent steep mountain valleys, the winds at Station Vito
187 (RSP) are coming off the Ross Ice Shelf, resulting in lower wind speed.

188 During the CTD sampling in the TNBP there were 4 periods of intense katabatic wind
189 events, with each event lasting for at least 24 hours or longer. During the CTD sampling in the
190 RSP there was just one event of near katabatic winds lasting about 24 hours. During each wind
191 event, the air temperature oscillated in a similar pattern and ranged from approximately -10 °C to
192 -30 °C.

193



194



195 Figure 3: Weather observations from 01 May to 17 May 2017. a.) Wind speed from Station
196 Manuela (blue line), Station Vito (purple line), NB Palmer (green line), and SWIFT (orange
197 marker) deployments adjusted to 10 meters. The commonly used katabatic threshold of 17 m s^{-1}
198 is depicted as a “dotted red line”, as well as the date and start time of each CTD cast. b) Air
199 temperature from Station Manuela, Station Vito, NB Palmer, and SWIFT deployments.
200
201

202 3. EVIDENCE OF FRAZIL ICE FORMATION

203

204 3.1 Selection of profiles

205

206 We used the following selection criteria to identify profiles from the two polynyas that
207 appeared to be influenced by frazil ice formation: (1) a deep mixed layer extending several



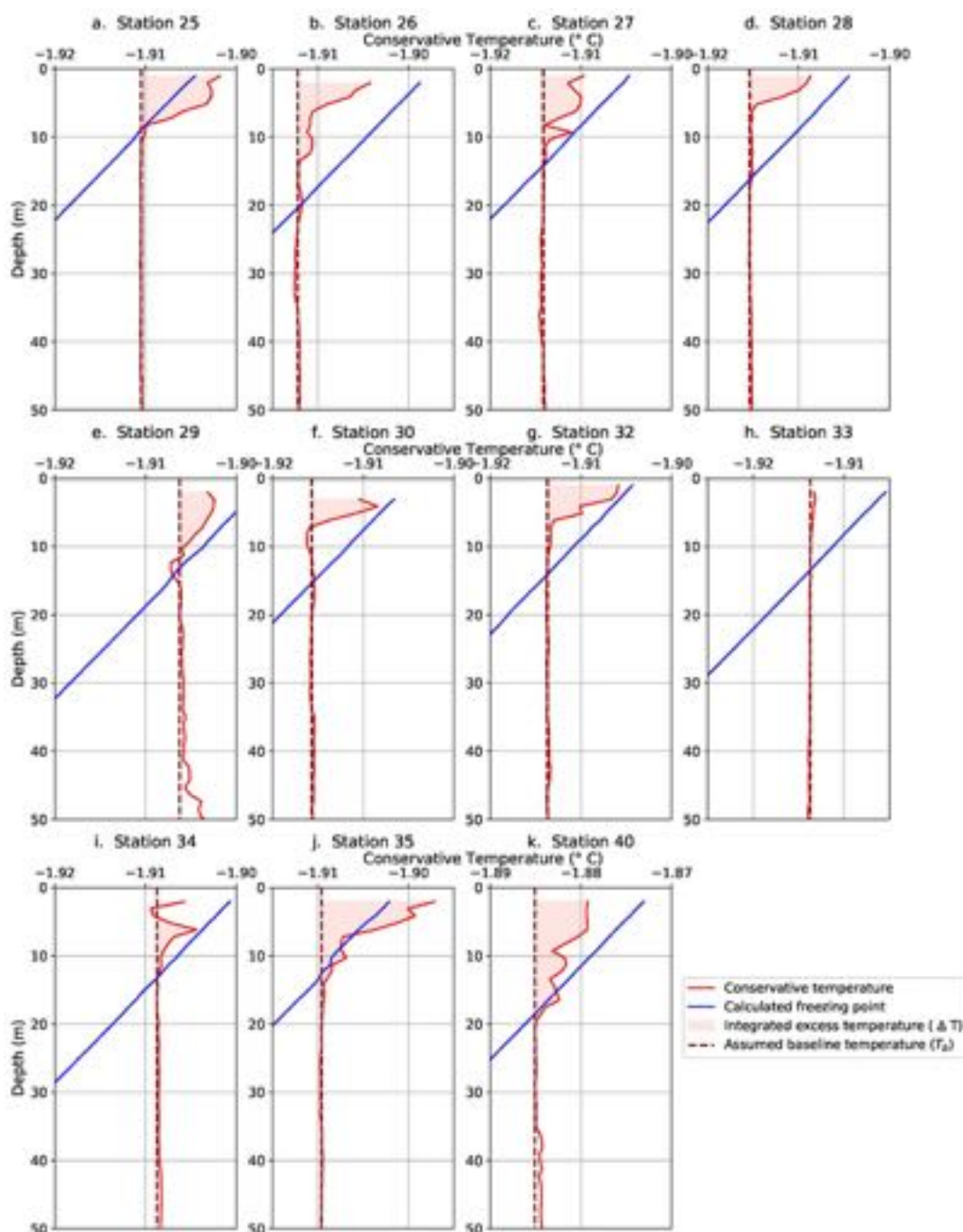
208 hundred meters (Supplemental Figure 1), (2) in-situ temperature readings below the freezing
209 point in the near-surface water (upper five meters), and (3) an anomalous bolus of warm and/or
210 salty water within the top twenty meters of the profile (Figure 4 and 5). For context, all
211 temperature profiles acquired during PIPERS (with the exception of one profile acquired well
212 north of the Ross Sea continental shelf area at 60°S, 170°E) were plotted to show how polynya
213 profiles compared to those outside of polynyas (Supplemental Figure 1).

214

215



216



Conservative temperature
Calculated freezing point
Integrated excess temperature (ΔT)
Assumed baseline temperature (T_0)

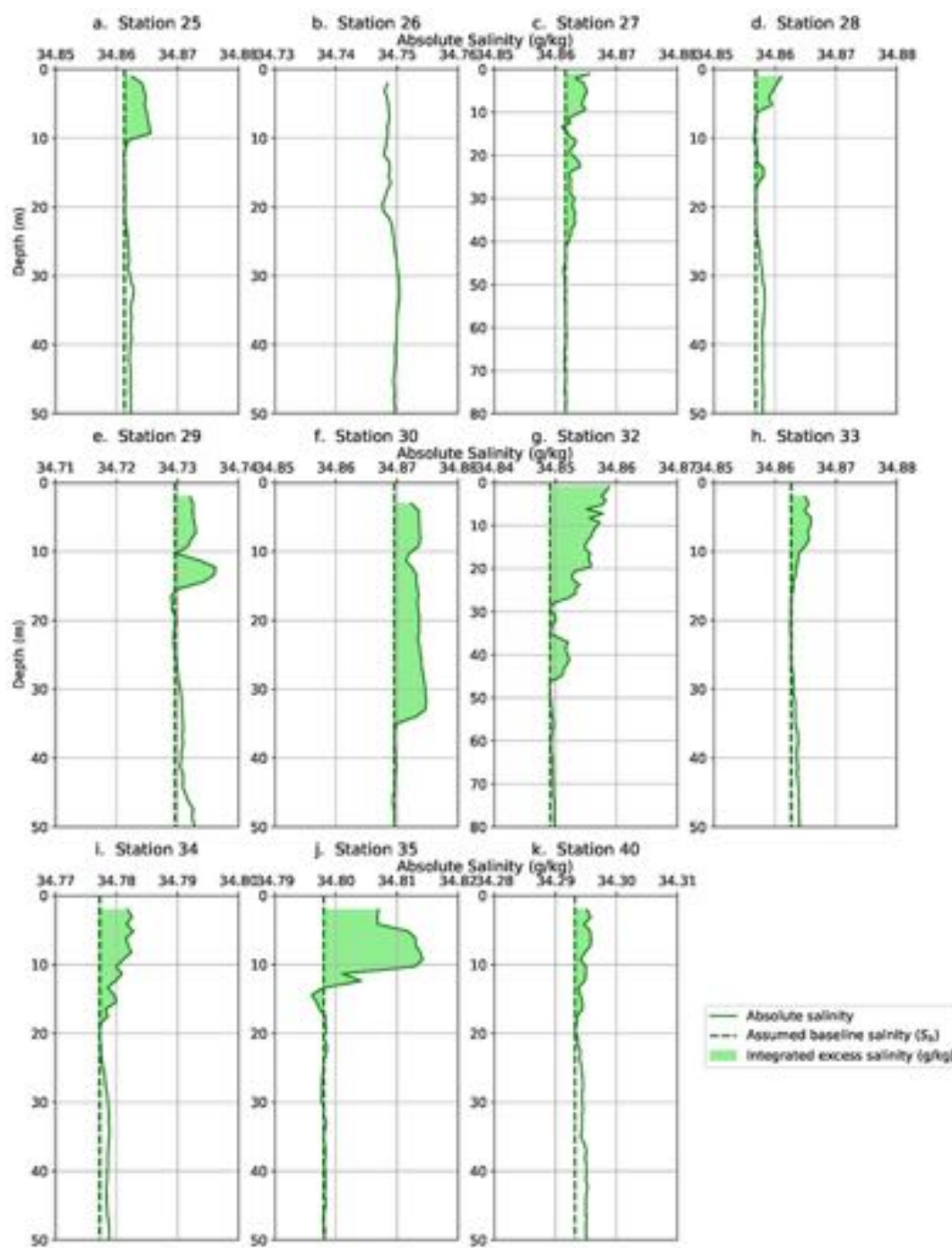


217 Figure 4: Conservative Temperature profiles from CTD down casts from 11 stations showing
218 temperature and/or salinity anomalies. Profiles (a-g) and (j-k) all show an anomalous
219 temperature bulge. They also show supercooled water at the surface with the exceptions of (a)
220 and (j). All of the plots (a- h) have an x-axis representing a 0.02 °C change. Profiles (a-j) are
221 from TNBP, and (k) is from RSP.

222 Polynya temperature profiles were then evaluated over the top 50 meters of the water
223 column using criteria 2 and 3. Nine TNBP profiles and one RSP profile exhibited the excess
224 temperature anomalies over the top 10-20 m and near-surface temperatures close to the freezing
225 point (Figure 4). Excess salinity anomalies (Figure 5) were observed at the same stations with
226 two exceptions: Station 26 had a measurable temperature anomaly (Figure 4b) but no discernible
227 salinity anomaly (Figure 5b), and Station 33 had a measurable salinity anomaly (Figure 5h) but
228 no discernible temperature anomaly (Figure 4h). The stations of interest are listed in Table 1.
229



230





231 Figure 5: Absolute Salinity profiles from CTD down casts from 11 stations showing temperature
232 and/or salinity anomalies. Profiles (a) and (c-k) show an anomalous salinity bulge in the top
233 10-20 meters. Two profiles (c and g) show salinity anomalies extending below 40 meters, so the
234 plot was extended down to 80 meters to best highlight those. All of the plots (a-k) have an
235 absolute salinity range of 0.03 g kg^{-1} .

236

237

238 **3.2 Evaluating the uncertainty in the temperature and salinity anomalies**

239

240 To evaluate the uncertainty associated with the temperature and salinity anomalies at each
241 of the polynya stations, we compared each anomaly to the initial accuracy of the SBE 911
242 temperature and conductivity sensors: $\pm 0.001 \text{ }^{\circ}\text{C}$ and $\pm 0.0003 \text{ S m}^{-1}$, or $\pm 0.00170 \text{ g kg}^{-1}$ when
243 converted to absolute salinity. To quantify the maximum amount of the temperature anomaly, the
244 baseline excursion, ΔT , was calculated throughout the anomaly $\Delta T = T_{\text{obs}} - T_b$, where T_{obs} is the
245 in-situ conservative temperature and T_b is the in-situ baseline, which is extrapolated from the far
246 field conservative temperature within the well-mixed layer below the anomaly. Taking the single
247 largest baseline excursion from each of the 11 anomalous CTD profiles and averaging them, we
248 compute an average baseline excursion of $0.0064 \text{ }^{\circ}\text{C}$. While this is a small change in the
249 temperature, it is still 32 times larger than the stated precision of the SBE 911 ($0.0002 \text{ }^{\circ}\text{C}$). The
250 same approach applied to the salinity anomalies yielded an average baseline of 0.0041 S m^{-1} (or
251 0.0058 g kg^{-1} for absolute salinity), which is 100 times larger than the instrument precision
252 (0.00004 S m^{-1}). Table 1 lists the maximum temperature and salinity anomalies for each CTD
253 station.

254 One concern was that frazil ice crystals could interfere with the conductivity sensor. It is
255 conceivable that ice crystals smaller than 5 mm can be sucked into the conductivity cell, creating
256 spikes in the raw conductance data. Additionally, frazil crystals smaller than $100 \mu\text{m}$ are
257 theoretically small enough to float between the electrodes and thereby decrease the
258 resistance/conductance that is reported by the instrument (Skogseth & Smedsrød, 2009). To test
259 for ice crystal interference, the raw (unfiltered with no bin averaging) absolute salinity profile



260 was plotted using raw conductivity compared with the 1-meter binned data for the 11 anomalous
261 CTD Stations (Supplemental Figure 2). The raw data showed varying levels of noise as well as
262 some spikes or excursions to lower levels of conductance; these spikes may have been due to ice
263 crystal interference. However, the bin-averaged data do not appear to be biased or otherwise
264 influenced by the spikes, which tend to fall symmetrically around a baseline. This was
265 demonstrated by bin-averaging over different depth intervals as described in §2.4. Considering
266 the consistency of the temperature and salinity measurements within and below the anomalies,
267 and the repeated observation of anomalies at 11 CTD stations, we infer that the observed
268 anomalies are not an instrumental aberration.

269

270 **3.3 Camera observations of frazil ice formation**

271

272 During PIPERS an EISCam (Evaluative Imagery Support Camera, version 2) was
273 operating in time lapse mode, recording photos of the ocean surface from the bridge of the ship
274 every 10 minutes (for more information on the EISCam see Weissling et al, 2009). The images
275 from the time in TNBP and RSP reveal long streaks and large aggregations of frazil ice. A
276 selection of photos from TNBP were captured (Figure 6). The winds were strong enough at all
277 times to generate wave fields and advect frazil ice, thus creating downstream frazil streaks, and
278 eventually pancake ice in most situations. Smaller frazil streaks and a curtain of frazil ice below
279 the frazil streak were also visible.

280

281

282



283

a. Photo from 04- May 23:00



b. Photo from 05- May 02:00



c. Photo from 05- May 01:00



d. Photo from 06- May 22:00



284

Figure 6: Images from NB Palmer as EISCam (Evaluative Imagery Support Camera) version 2. White areas in the water are loosely consolidated frazil ice crystals being actively formed during a katabatic wind event. Image (d) was brightened to allow for better contrast.

285

288 3.4 Conditions for frazil ice formation during lab experiments

289

Ushio and Wakatsuchi (1993) conducted laboratory experiments to reproduce the conditions observed in polynyas. They exposed their tank, measuring 2-m length, 0.4-m width and 0.6-m depth to air temperatures at -10°C and wind speeds of 6 m s^{-1} . They observed supercooling in the range of 0.1 to 0.2°C at the water surface and found that after 20 minutes the rate of super-cooling slowed due to the release of latent heat, coinciding with visually observed frazil ice formation. Simultaneously with the formation of frazil ice crystals, they observed an increase in salinity from the brine rejection. After ten minutes of ice formation, the temperature of the frazil ice layer was 0.07°C warmer and the layer was 0.5 to 1.0% saltier (Ushio and Wakatsuchi, 1993).



298 In this study, we found the frazil ice layer to be on average 0.0064 °C warmer than the
299 underlying water. Similarly, the salinity anomaly was on average 0.0058 g kg⁻¹ saltier, which
300 equates to 0.017% saltier than the water below. While our anomalies were significantly smaller
301 than those observed in the lab tank by Ushio and Wakatsuchi (1993), the same trend of
302 super-cooling, followed by frazil ice formation and the appearance of a salinity anomaly was
303 observed during PIPERS. However, the forcing conditions and spatial constraints of the tank
304 experiment likely explain why there are discrepancies between the magnitudes of the
305 temperature and salinity anomalies observed in the lab versus in the field.

306

307 **3.5 Temperature and salinity profiles in the presence of platelet ice formation**

308 The mechanism for supercooling under ice shelves occurs via a different process than in
309 polynyas, but with similar impact on the water column structure. In polynyas, katabatic winds
310 and sub-freezing air temperatures create supercooled water near the surface, which drove frazil
311 ice formation. As plumes of Ice Shelf Water approached the surface, the pressure change led to
312 the formation of supercooled water and frazil ice formation (Jones & Wells, 2018). Robinson et
313 al (2017) investigated ice formation through this process under the McMurdo Sound Ice Shelf.
314 As the frazil crystals continue to grow, they maintained their geometry and formed platelet ice.
315 Robinson et al. (2017) found an increase in salinity from brine rejection and an increase in
316 temperature from latent heat released at the depth of ice formation. Though the mechanism for
317 supercooling differs, these vertical trends in temperature and salinity nonetheless are similar to
318 our results.

319

320 **3.6. The anomalous profiles from TNBP and RSP appear to trace active frazil ice 321 formation**

322

323 Throughout Sections 2 and 3, we have documented that the anomalous profiles from
324 TNBP and RSP appear to trace frazil ice formation. In §2.4, the strong winds and sub-zero air
325 temperatures supported both ice formation and advection. In §3.1 and §3.2, we showed that the
326 CTD profiles in both temperature and salinity are reproducible and large enough to be



327 distinguished from the instrument noise. In §3.3 the coincident EISCam measurements reveal
328 significant accumulation of frazil ice crystals on the ocean surface during the time the NB
329 Palmer was in TNBP and RSP. In §3.4 and §3.5, we note the commonalities between the PIPERS
330 polynya profiles and frazil ice formation during platelet ice formation and during laboratory
331 experiments of frazil ice formation. Given the co-occurrence of strong winds, cold air
332 temperatures, sub-zero water temperature, we find no simpler explanation for the apparent
333 warmer, saltier water near the surface in our 11 CTD profiles from TNBP and RSP. Considering
334 the similarity in conditions during the lab experiments and during in-situ platelet ice formation,
335 we conclude that our 11 profiles reflect measurable frazil ice formation in the TNBP and RSP.
336

337 **4.0 ESTIMATION OF FRAZIL ICE CONCENTRATION USING CTD PROFILES**

338

339 Having identified a collection of CTD profiles that trace frazil ice formation, we want to
340 know how much frazil ice formation can be inferred from these T and S profiles? Can we
341 attribute a large portion of polynya ice formation to this early stage of ice growth, or is the
342 growth of pack ice at the polynya edge the dominant process? To estimate ice formation, the
343 inventories of heat and salt from each profile can provide independent estimates of frazil ice
344 concentration. To simplify the inventory computations, we neglect the horizontal advection of
345 heat and salt; this is akin to assuming that lateral variations are not important because the
346 neighboring water parcels are also experiencing the same intense vertical gradients in heat and
347 salt. We first describe the computation using temperature in § 4.1 and the computation using
348 salinity in § 4.2.

349

350 **4.1 Estimation of frazil ice concentration using temperature anomalies**

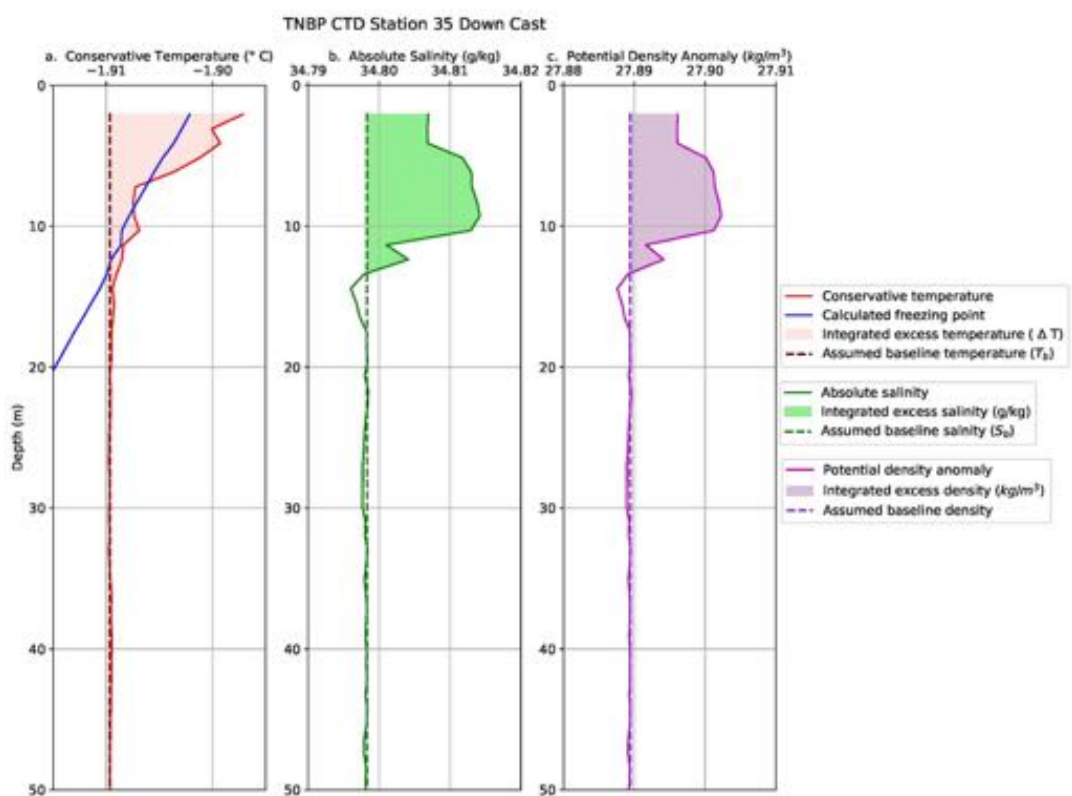
351

352 We used the temperature profiles to compute the “excess” heat inside the anomalies.
353 Utilizing the latent heat of fusion as a proxy for frazil ice production we estimated the amount of
354 frazil ice that must be formed in order to create observed anomalies. For each station, we first
355 estimated the enthalpy inside the temperature anomaly (Talley et al, 2011) as follows. Within
356 each CTD bin, we estimated the excess temperature as $\Delta T = T_{\text{obs}} - T_b$, where T_{obs} is the in-situ



356 conservative temperature and T_b is the in-situ baseline or far field conservative temperature. The
357 excess over the baseline is graphically represented in Figure 7a. Because we lacked multiple
358 profiles at the same location, we were not able to observe the time evolution of these anomalies.
359 Consequently, T_b represents our best inference of the temperature of the water column prior to
360 the onset of ice formation; it is highlighted in Figure 7a with the dashed line. We established T_b
361 by looking for a near constant value of temperature in the profile directly below the temperature
362 bulge. In most cases the temperature trend was nearly linear and close to the freezing point.
363 After selecting the starting location, the conservative temperature was averaged over 10 meters
364 (10 values from the 1-m binned data) to eliminate slight variations and any selection bias.

365



366 Figure 7: Conservative temperature, absolute salinity, and potential density anomaly for TNBP
367 CTD Station 35, May 10, 2017. a) Conservative temperature profile showing the temperature
368 anomaly, the selected baseline temperature (dashed line) and the integrated excess temperature
369 (shaded area). b) Absolute salinity profile showing the salinity anomaly, the selected baseline



370 salinity (dashed line), and integrated excess salinity (shaded area). c) Potential density anomaly
371 showing the selected baseline density (dashed) and the excess density instability (shaded).
372

373 To find the excess heat (Q_{excess}^{total}) represented in the total thermal anomaly, we computed
374 the vertical integral of heat per unit area from the surface ($z=0$) to the bottom of the anomaly
375 ($z=z_T$):

$$376 Q_{excess}^{total} = \int_{z=0}^{z=z_T} \rho C_p \Delta T dz \quad (1)$$

377 Here ρ = density of seawater, z = the depth range of the anomaly, and C_p = the specific heat
378 capacity, The concentration of frazil ice is estimated by applying the latent heat of formation (L_f
379 = 330 kJ kg⁻¹) as a conversion factor to Q_{excess}^{total} :

$$380 Conc_{ice}^{temp} = \frac{Q_{excess}^{total}}{L_f * z_T} \quad (2)$$

381 Where z_T is the depth of the temperature anomaly in meters. The concentration of ice derived
382 represents the total concentration of ice, in kg m⁻³. A more detailed explanation of equations 1
383 and 2 is contained in Supplemental 1. The mass concentration of ice derived from the
384 temperature anomaly for each station is listed in Table 1.

385

386 4.2 Estimation of frazil ice concentration using salinity anomalies

387

388 The mass of salt within the salinity anomaly was used to estimate ice formation.
389 Assuming that frazil ice crystals do not retain any brine and assuming there is no evaporation,
390 the salinity anomaly is directly proportional to the ice formed. By using the conservation of mass
391 equations for water and salt, the mass of frazil ice can be estimated by comparing the excess salt
392 (measured as salinity) with the amount of salt initially present in the profile. The conservation of
393 mass equations used and subsequent derivations are in Supplemental 2. The salinity anomaly
394 (ΔS) above the baseline salinity (S_b) is $\Delta S = S_{obs} - S_b$, and is shown in Figure 7b. The initial
395 value of salinity (S_b) was established by observing the trend in the salinity profile directly
396 below the haline bulge; in most cases the salinity trend was nearly linear beneath the bulge,



397 however in general the salinity profiles were less homogeneous than the temperature profiles.
398 After selecting the starting location from below the anomaly, the absolute salinity was averaged
399 over the next 10 meters to establish a baseline salinity.

400 To find the total mass of frazil ice ($Mass_{ice}^S$, kg m⁻²) in the water column, the integral of
401 each component of the salt ratio is taken over the depth range of the anomaly. This integral is
402 multiplied by the total mass of water per area ($Mass_{Water}^{Total}$, kg m⁻²) initially in the depth range of
403 the anomaly. The concentration of ice ($Conc_{Ice}^{salt}$, kg m⁻³) can be found by dividing the mass of
404 frazil ice by the depth of the salinity anomaly (z_s). The resulting estimates of ice concentration
405 are listed in Table 1.

406

$$Mass_{ice}^S = Mass_{Water}^{Total} * \frac{\int_{z=0}^{z=H} \Delta S dz}{\int_{z=0}^{z=H} S_{obs} dz} \quad (3)$$

407

$$Mass_{Water}^{Total} = \rho_b * \int_{z=0}^{z=H} dz \quad (4)$$

408

$$Conc_{Ice}^{salt} = \frac{Mass_{ice}^S}{z_s} \quad (5)$$

409 A more detailed explanation of equations 3, 4, and 5 is contained in Supplemental 3.
410

411 4.3 Summary of the frazil ice estimates

412

413 The derived ice concentrations are listed in Table 1. The inventories of salt produced
414 in-situ frazil ice concentrations from 24×10^{-3} kg m⁻³ to 332×10^{-3} kg m⁻³. However, it is
415 noteworthy that the estimates of frazil ice concentration from salt inventories are anywhere from
416 2 to 9 times greater than the estimates from heat inventories. The difference is likely produced by
417 unquantified heat loss to the atmosphere. The influence of sensible and long wave heat
418 exchanges produces an atmospheric loss term in the heat inventory, which has no corresponding
419 influence on the salt inventory. Therefore, we suggest that derived ice concentrations from the
420 heat anomalies underestimated frazil ice concentration in comparison to the salt inventory.

421 We also note the salinity calculation does not account for evaporation. However,
422 evaporation could have contributed to excess salinity while simultaneously decreasing the



423 temperature. Mathiot et al. (2012) found that evaporation was secondary to ice production and
424 contributed 4% to salt flux. In the TNBP, the Palmer meteorological tower revealed high relative
425 humidity (on average 78.3%), so the effects of evaporation on salinity were likely therefore
426 negligible. The effects of evaporation would reduce the mass of ice derived from the salinity
427 anomaly.

428

429 Table 1: CTD Stations with temperature and salinity anomalies (See Figures 4-5), showing
430 maximum values of the temperature anomaly, depth range of the temperature anomaly,
431 concentration of ice derived from the temperature anomaly (§4.1), as well as the maximum value
432 of the salinity anomaly, depth range of salinity anomaly, and concentration of ice derived from
433 the salinity anomaly (§4.2).

Station	Date and Time	Maximum ΔT (°C)	z_T (m)	$Conc_{ice}^T$ (kg m ⁻³)	Maximum ΔS (g kg ⁻¹)	z_S (m)	$Conc_{ice}^S$ (kg m ⁻³)
25	May 03 23:00:41	0.009	11.34	48.85×10^{-3}	0.004	13.4	77.76×10^{-3}
26*	May 06 02:30:08	0.008	24.73	16.42×10^{-3}	--	--	--
27	May 06 13:08:11	0.005	15.45	22.59×10^{-3}	0.003	41.22	48.01×10^{-3}
28	May 06 17:59:12	0.007	15.52	17.85×10^{-3}	0.004	17.52	24.37×10^{-3}
29	May 07 15:29:32	0.004	11.34	22.05×10^{-3}	0.007	21.64	58.55×10^{-3}
30	May 09 07:28:24	0.007	8.24	24.88×10^{-3}	0.005	36.07	116.63×10^{-3}



32	May 09 18:24:56	0.008	11.33	32.39×10^{-3}	0.007	47.4	121.90×10^{-3}
33**	May 10 05:16:29	---	---	---	0.004	22.67	32.38×10^{-3}
34	May 10 20:16:46	0.004	13.4	9.63×10^{-3}	0.005	19.58	80.29×10^{-3}
35	May 11 00:56:32	0.012	19.58	35.65×10^{-3}	0.016	14.43	332.16×10^{-3}
40	May 17 04:02:37	0.006	20.61	34.21×10^{-3}	0.003	18.55	48.84×10^{-3}

434 *Station 26 did not have a measurable salinity anomaly but was included due to the clarity of the
435 temperature anomaly. Conversely, **Station 33 did not have a measurable temperature anomaly
436 but was included due to the clarity of the salinity anomaly.

437

438 5.0 ESTIMATION OF TIME SCALE OF ICE PRODUCTION

439

440 How should we interpret the lifetime of these T and S anomalies? Are they short-lived in the
441 absence of forcing, or do they represent an accumulation over some longer ice formation period?
442 One possibility is that the anomalies begin to form at the onset of the katabatic wind event,
443 implying that the time required to accumulate the observed heat and salt anomalies is similar to
444 that of a katabatic wind event (e.g. 12-48 hours). This, in turn would suggest that the estimated
445 frazil ice production occurred over the lifetime of the katabatic wind event. Another
446 interpretation is that the observed anomalies reflect the near-instantaneous production of frazil
447 ice. In this scenario, heat and salt are simultaneously produced and actively mixed away into the
448 far field. In this case, the observed temperature and salinity anomalies reflect the net difference
449 between production and mixing. One way to address the question of lifetime is to ask “if ice
450 production stopped, how long would it take for the heat and salt anomalies to dissipate?” The



451 answer depends on how vigorously the water column is mixing In this section, we examine the
452 mixing rate. However, we can first get some indication of the timescale by the density profiles.
453

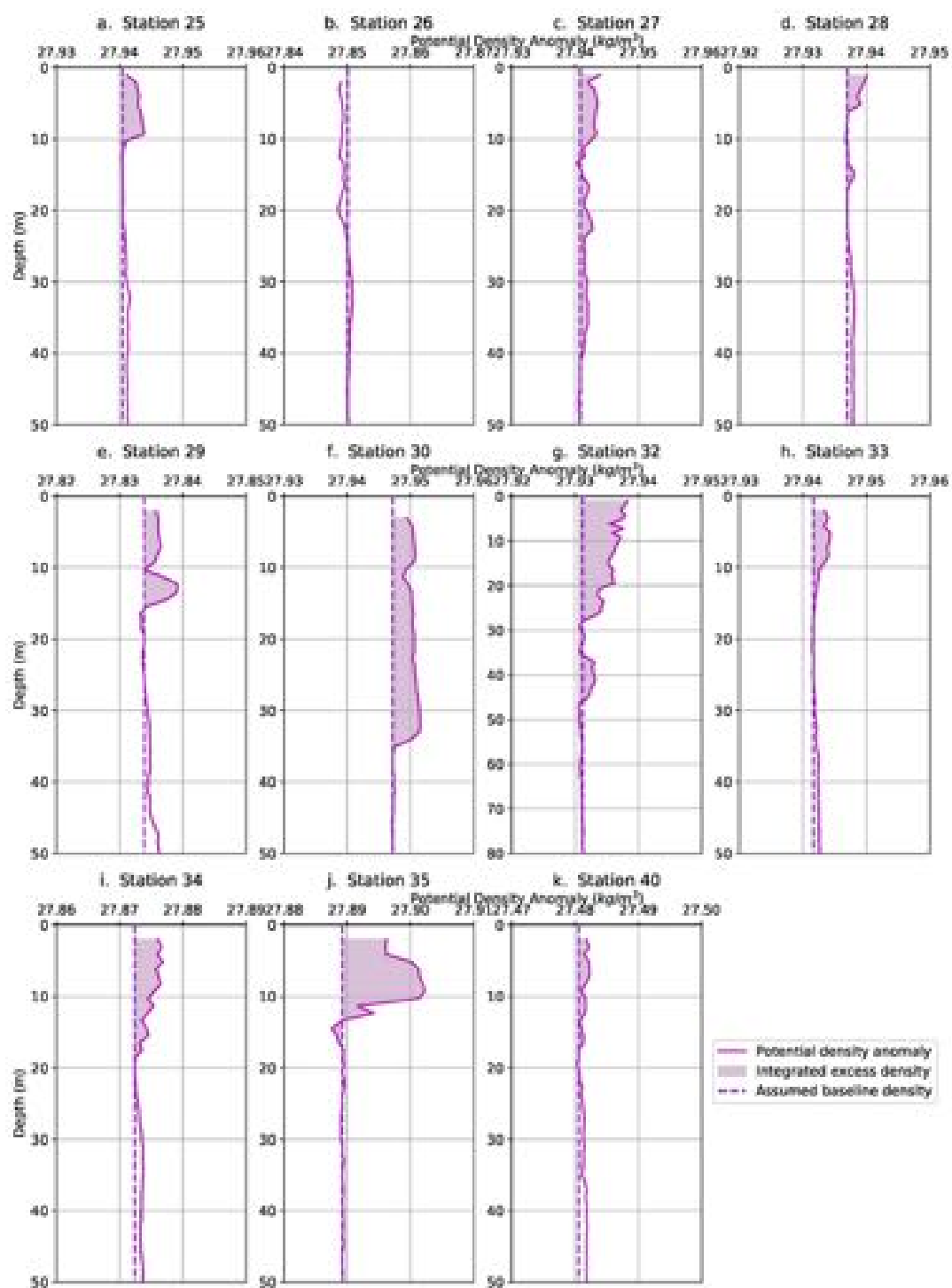
454 **5.1 Apparent instabilities in the density profiles**

455

456 The computed density profiles reveal an unstable water column for all but one of our
457 eleven stations (Figure 8). These suggest that buoyancy production from excess heat did not
458 effectively offset the buoyancy loss from excess salt within each anomaly. It is not common to
459 directly observe water column instability without the aid of microstructure or other instruments
460 designed for measuring turbulence.



461





462 Figure 8: Potential density anomalies for all 11 stations with evidence of active frazil ice
463 formation. The integrated excess density and assumed baseline density are depicted to highlight
464 the instability. Note that Station 26 (b) does not present a density anomaly because it does not
465 have a salinity anomaly. In the absence of excess salinity, the temperature anomaly created
466 instead an area of less dense water (i.e., a stable anomaly).

467

468 We suggest that an instability in the water column that persists long enough to be
469 measured in a CTD profile, must be the result of a continuous buoyancy loss that is created at a
470 rate faster than it can be eroded by mixing. In other words, the katabatic winds appeared to
471 dynamically maintain these unstable profiles. Continuous ice production leads to the production
472 of observed heat and salt excesses at a rate that exceeds the mixing rate. If the unstable profiles
473 reflect a process of continuous ice production, then the inventory of ice that we infer from our
474 simple heat and salt budgets must reflect ice production during a relatively short period of time,
475 defined by the time it would take to mix the anomalies away, once the wind-driven dynamics and
476 ice production stopped.

477 Similarly, Robinson et al (2017) found that brine rejection from platelet ice formation
478 (§3.5) also leads to dense water formation and a static instability. Frazil ice formation from
479 continually supplied ISW created a stationary instability, which was observable before being
480 mixed by convection to the underlying homogeneous water column that extended to 200 meters.
481 Similarly, the katabatic winds and cold air temperatures continually supply supercooled water to
482 the polynya supporting the instability.

483

484 **5.2 Lifetime of the salinity anomalies from Monin-Obukhov length scale**

485

486 Turbulence theory suggests the largest eddies control the rate of turbulence dissipation
487 (Cushman-Rosin, 2019). A characteristic timescale, t , can be approximated by relating the largest
488 eddy size and the rate of turbulent kinetic energy dissipation (ϵ , Cushman-Rosin, 2019).

489
$$t \approx \frac{d}{(\epsilon d)^{\frac{1}{3}}} \approx \left(\frac{d^2}{\epsilon}\right)^{\frac{1}{3}} \quad (6)$$



490 Here, d is the characteristic length of the largest eddy and ε is the turbulent kinetic energy
491 dissipation rate. In this section we discuss and select the best length scale for an environment
492 dominated by buoyancy and wind shear. We use observed parameters to estimate the terms in
493 equation (6).

494 The dimension, d , of the largest eddy in a vigorously mixing water column could be
495 equivalent to the scale of the domain (in this case, the mixed layer depth) which was up to 600 m
496 in some of the PIPERS profiles (Table 2). However, a homogenous mixed-layer does not
497 necessarily imply active mixing throughout the layer (Lombardo and Gregg, 1989). Instead, the
498 characteristic length scale in an environment driven by both buoyancy and wind shear is
499 typically the Monin-Obukhov length (L_{M-O}) (Monin & Obukhov, 1954). When L_{M-O} is small
500 and positive, buoyant forces are dominant and when L_{M-O} is large and positive, wind shear
501 forces are dominant (Lombardo & Gregg, 1989). While the L_{M-O} can be expressed using several
502 different estimates of shear and buoyancy, we focus on the salt-driven buoyancy flux, because
503 those anomalies come closest to capturing the process of frazil ice production (see §4.3 for more
504 detail).

505

506
$$L_{M-O} = - \frac{u_*^3}{k\beta gw\overline{\Delta S}} \quad (7)$$

507

508 where u_* is the wind-driven friction velocity at the water surface, g is gravitational acceleration,
509 w is the water vertical velocity, $\overline{\Delta S}$ is the salt flux, β is the coefficient of haline contraction, and
510 k is the von Karman constant. A more detailed explanation, along with the specific values are
511 listed in Supplemental 4.

512 Wind-driven friction velocity is estimated using the NB Palmer wind speed (U_{palmer})
513 record from a masthead height of $z_{palmer} = 24$ m, adjusted to a 10 meter reference (U_{10}) by
514 assuming a logarithmic profile (Manwell et al., 2010).

515

516
$$U_{10} = U_{palmer} * \frac{\ln(\frac{z_0}{z_{palmer}})}{\ln(\frac{z_{palmer}}{z_0})} \quad (8)$$

517



518 Roughness class 0 was used in the calculation and has a roughness length of 0.0002 m. These
519 values are used to estimate the wind stress, τ as,

520
$$\tau = C_D \rho_{air} U_{10}^2 \quad (9)$$

521

522 where ρ_{air} represents the density of air, with a value of 1.3406 kg m^{-3} calculated using averages
523 from NB Palmer air temperature (-18.73°C), air pressure (979.4 mbars) and relative humidity
524 (78.3%). C_D represents a dimensionless drag coefficient and was calculated as 1.525×10^{-3} ,
525 using COARE 3 code, modified to incorporate wave height and speed (Fairall et al, 2003). The
526 average weather data from NB Palmer was paired with the wave height and wave period from
527 the SWIFT deployment (defined below) on 04 May to find C_D . A more detailed explanation and
528 the specific values are listed in Supplemental 5.

529

530 We determined the aqueous friction velocity (u_*) at the air-sea interface using:

531
$$u_* = \sqrt{\frac{\tau}{\rho_{water}}} \quad (10)$$

532

533 We used a SWIFT (Surface Wave Instrument Float with Tracking) buoy to provide
534 estimates of turbulent kinetic energy dissipation and vertical velocity. (Thomson et al., 2016;
535 Zippel & Thomson, 2016). SWIFT deployments occurred during the period of CTD
536 observations, as shown in the timeline of events (Supplemental Figure 3). The SWIFT
537 deployments do not always coincide in time and space with the CTD profiles. For the vertical
538 velocity estimation we identified the May 04 and May 09 SWIFT deployments as most relevant
539 to CTD stations analyzed here based on similarity in wind speeds. The average wind speed at all
540 the CTD stations with anomalies was 10.2 m s^{-1} . For the May 4 SWIFT deployment, the wind
541 speed was 9.36 m s^{-1} . CTD Station 32, more than two standard deviations from the average,
542 experienced the most intense winds of the CTD stations at 18.9 m s^{-1} . For CTD Station 32, the
543 May 9 SWIFT deployment was used, which had a wind speed of 20.05 m s^{-1} . For May 04 and
544 May 09, the average vertical velocity (w) was measured in the upper meter of the column. May
545 04 had an average value of $w = 0.015 \text{ m s}^{-1}$. May 09 had an average value of $w = 0.025 \text{ m s}^{-1}$. See



546 Thomson et al., 2016 & Zippel & Thomson, 2016 for details on how these measurements are
547 made.

548 The TKE dissipation rates are expected to vary with wind speed, wave height, ice
549 thickness and concentration (Smith & Thomson, 2019). Wind stress (τ_{wind}) is the source of
550 momentum to the upper ocean, but this is modulated by scaling parameter (c_e , Smith &
551 Thomson, 2019). If the input of TKE is in balance with the TKE dissipation rate over an active
552 depth layer, the following expression can be applied:

553

$$c_e * \tau_{wind} \propto \rho \int \epsilon(z) dz \quad (11)$$

554

555 where the density of water (ρ) is assumed to be 1027 kg m^{-3} for all stations. The scaling
556 parameter incorporates both wave and ice conditions; more ice produces more efficient wind
557 energy transfer, while simultaneously damping surface waves, with the effective transfer velocity
558 in ice, based on the assumption that local wind input and dissipation are balanced (Smith &
559 Thompson, 2019).

560

561

$$c_e = a (A \frac{z_{ice}}{H_s})^b \quad (12)$$

562 Here, A is the fractional coverage of ice, with a maximum value of 1, z_{ice} is the thickness of ice,
563 and H_s is the significant wave height. Using Antarctic Sea ice Processes and Climate or ASPeCt
564 visual ice observations (www.aspect.aq) from NB Palmer, the fractional ice cover and thickness
565 of ice were found at the hour closest to both SWIFT deployments and CTD profiles (Knuth &
566 Ackley, 2006; Ozsoy-Cicek et al., 2008; Worby et al., 2008). The significant wave height for
567 each SWIFT deployment was used. We lacked time series data for H_s during the time of CTD
568 casts, so the average value from May 04 of 0.58 m was used for all the CTD profiles. To get the
569 most robust data set possible, in total, 13 vertical SWIFT profiles from May 2, May 4, and May
570 9 were used to evaluate equation 12 over an active depth range of 0.62 meters.

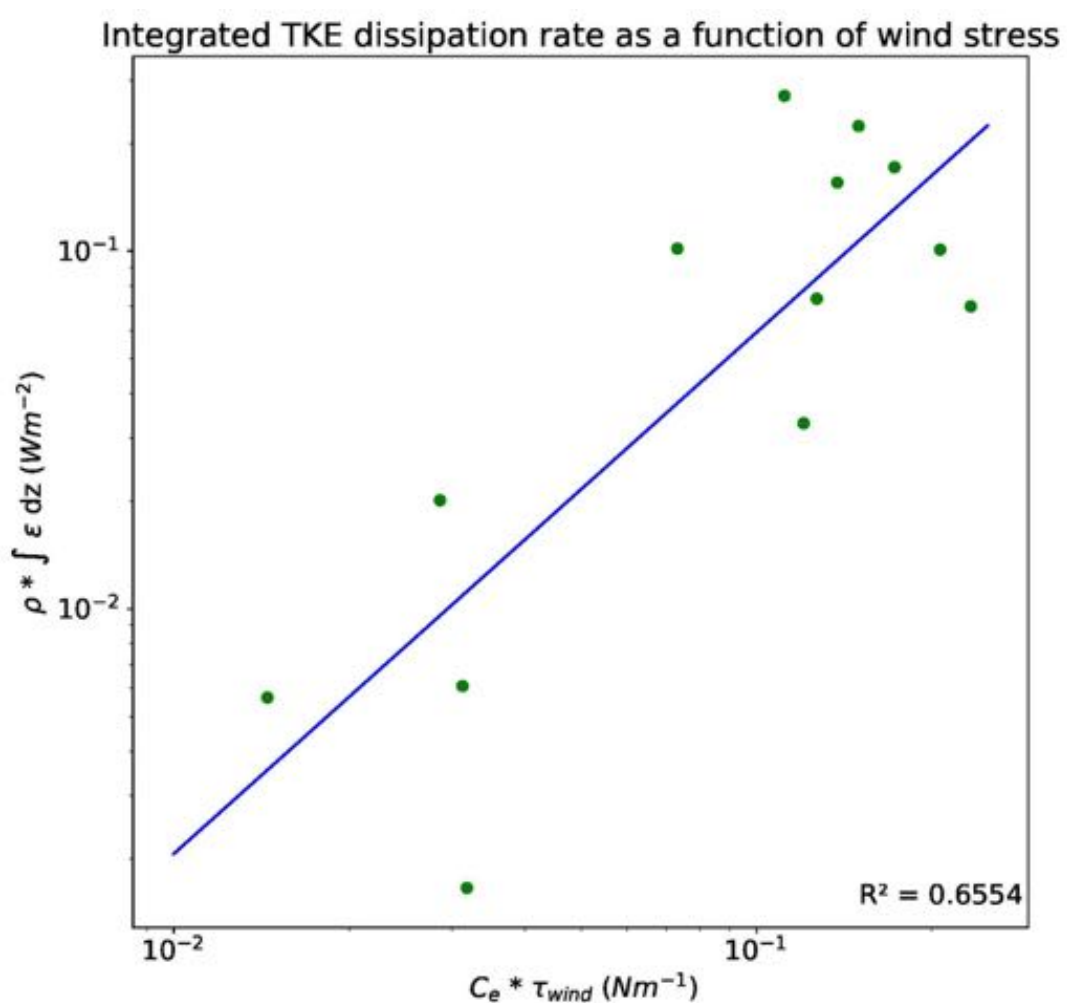
571

572 Using the estimates of c_e , τ , and ϵ from the SWIFT, we parameterized the relationship between
573 wind stress and ϵ that is reflected in equation (11). A log-linear fit ($y = 10^{(1.4572 * \log_{10}(x) + 0.2299)}$,



574 $r^2 = 0.6554$) was then applied to NB Palmer wind stress data to derive turbulent kinetic
575 dissipation estimates that coincided with the ambient wind conditions during each CTD station
576 (Table 2).

577



578 Figure 9: Logarithmic linear fit of the input flux of TKE into the ocean versus the TKE
579 dissipation rate over the active depth range.

580

581 Following estimation of the environmental parameters, Equation 7 can now be used to
582 estimate L_{M-O} . For these calculations a value of 0.41 was used for the von Karman constant, k .
583 Haline contraction, β , was calculated from Gibbs Seawater toolbox and averaged over the depth



584 range of the anomaly. The excess salt, $\overline{\Delta S}$, was found using the average value of ΔS for each
585 profile anomaly. The values of L_{M-O} range from 6 m to 330 m (Table 2). In general, L_{M-O} was
586 greater than the length of the salinity anomaly but smaller than the mixed layer depth. Using
587 L_{M-O} and the estimates of ϵ , the characteristic lifetime of the salinity anomalies ranged from 2
588 to 12 minutes, but most values cluster near the average of 9 min. The average timescale is similar
589 to the frazil ice lifetime found in Michel (1967). These lifetimes suggest that frazil ice production
590 and the observed density instabilities relax to a neutral profile within ten minutes of a diminution
591 in wind forcing.

592

593 6.0 RATE OF FRAZIL ICE PRODUCTION

594

595 We can extend the analysis of anomaly lifetime to estimate a frazil ice production rate by
596 invoking the prior assumption of steady state TKE forcing and dissipation. In this case, the mass
597 of ice reflected by the salinity anomaly ($Conc_{ice}^{salt}$, in kg m^{-3}) was produced during the time
598 interval corresponding to the mixing lifetime (t) that was determined from TKE dissipation in
599 §5.2.

600

601
$$Production\ rate = \frac{Conc_{ice}^{salt} * z_s}{t * Q_{ice}} \quad (13)$$

602 Here, $Q_{ice} = 920 \text{ kg m}^{-3}$, t =lifetime, in days, and z_s = the depth of the salinity anomaly (m).
603 The results are summarized in Table 2. A more detailed explanation and the specific values are
604 listed in Supplemental 6.

605

606 6.1 Variability in the frazil ice production rate

607

608 The ten estimates of frazil ice production rate, expressed as ice thickness per unit time,
609 ranged from 7 to 378 cm day^{-1} . These frazil ice production rates show some spatial trends across
610 the Terra Nova Bay polynya that correspond with variable environmental conditions in different
611 sectors of the polynya. As shown in Figure 10, a longitudinal gradient emerges along the axis of
612 the TNBP when looking at a subsection of stations under similar wind conditions Station 30



613 ($U_{10}=11.50 \text{ m s}^{-1}$), Station 27 ($U_{10}=10.68 \text{ m s}^{-1}$), and Station 25 ($U_{10}=11.77 \text{ m s}^{-1}$). Beginning
614 upstream near the Nansen Ice shelf (Station 30) and moving downstream along the predominant
615 wind direction toward the northeast, the ice production rate decreases. The upstream production
616 rate is $69.38 \text{ cm day}^{-1}$ followed by midstream values of $28.43 \text{ cm day}^{-1}$, and lastly downstream
617 values of 9.83 cm day^{-1} . This pattern is similar to the pattern modeled by Gallee (1997). The
618 production rate at Station 35, was significantly higher than that at all other stations, but this large
619 excess is reflected in both the heat and salt anomalies. The salt inventory at station 35 is a factor
620 of 2.6 greater than the nearest station (Station 34), and profiles 34 and 35 were separated in time
621 by less than 5 hours. This other variations in ice production rate may reflect real variability
622 brought on by submesoscale fronts, eddies and other flow structures that are not easily captured
623 by coarse sampling.

624 We used the student t-distribution to derive confidence intervals for TKE dissipation rate
625 at each CTD station was used to bound the range of ice production rates, which are reported in
626 Table 2. Uncertainty in the heat and salt inventories were not included in the uncertainty
627 estimates, because we observed negligible difference in the inventory while testing the inventory
628 for effects associated with bin averaging bin averaging of the CTD profiles (Section 2.3).
629 Another small source of error arises from the neglect of evaporation. To quantify the amount of
630 error introduced by that assumption, we used the bulk aerodynamic formula for latent heat flux
631 and found the effects of evaporation across the CTD stations to be 1.8% [0.07-3.45%] (Zhang,
632 1997). This error due to the effects of evaporation found are similar to Mathiot et al (2012). On
633 average, the lower limit of ice production was 30% below the estimate and the upper limit was
634 some 44% larger than the estimated production.

635

636 Table 2: Summary of mass of ice derived from salinity, lifetime, and production rates.

Station	$Conc_{ice}^S$ (kg m^{-3})	z_s (m)	L_{M-O} (m)	TKE diss. ϵ ($\text{m}^2 \text{ s}^{-3}$)	Est MLD (m)	Lifetime (min)	Production rate (cm day^{-1})	Production rate 95% CI (cm day^{-1})



25	77.76×10^{-3}	13. 4	140.59	9.648×10^{-5}	350	9.83	16.60	[12.16 - 22.66]
26*	--	--	--	7.191×10^{-5}	100	--	--	--
27	48.01×10^{-3}	41. 2	151.26	8.188×10^{-5}	500	10.90	28.43	[20.98 - 38.51]
28	24.37×10^{-3}	17. 5	54.12	1.622×10^{-5}	600	9.42	7.09	[4.40 - 11.45]
29	58.55×10^{-3}	21. 6	80.00	5.375×10^{-5}	275	8.20	24.19	[17.75 - 32.96]
30	116.63×10^{-3}	36	83.45	3.771×10^{-5}	500	9.49	69.38	[49.34 - 97.55]
32	121.90×10^{-3}	47	197.03	3.466×10^{-4}	375	8.03	112.57	[68.25 - 185.69]
33	32.38×10^{-3}	23. 7	98.38	2.844×10^{-5}	500	11.64	9.87	[6.76 - 14.43]
34	80.29×10^{-3}	19. 6	65.56	6.397×10^{-5}	175	6.78	36.31	[26.83 - 49.14]
35	332.16×10^{-3}	14. 4	6.30	2.343×10^{-5}	150	1.99	377.69	[250.51 - 569.44]
40	48.84×10^{-3}	18. 6	174.61	9.603×10^{-5}	120	11.37	12.47	[9.14 - 17.02]

637 *Station 26 did not have a measurable salinity anomaly but was included due to the clarity of the
 638 temperature anomaly.

639



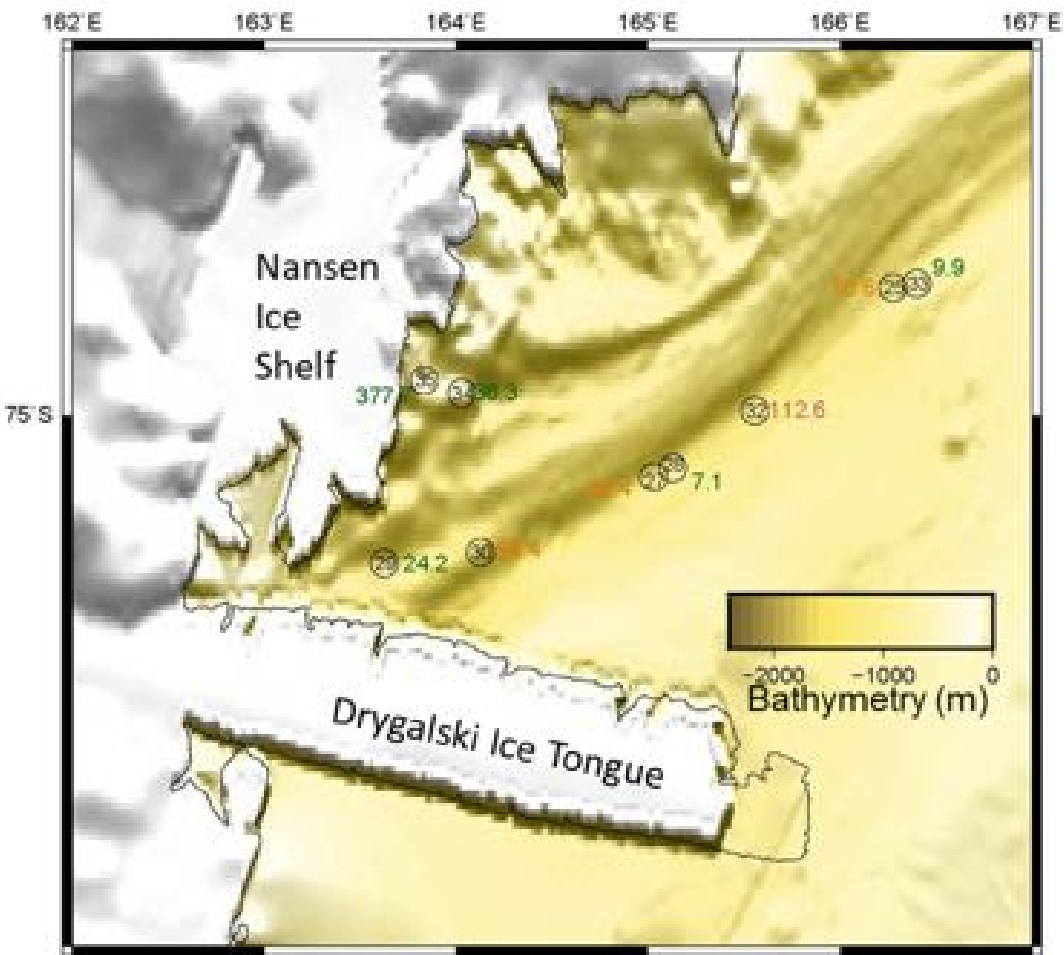
640

641 **6.2 Comparison to prior model and field estimates of ice production**

642 Calculated production rates from PIPERS ranged from 7 to 378 cm day⁻¹ (Figure 10). The
643 median ice production rate, 26.31 cm day⁻¹, is similar to Schick (2018), who estimated an
644 average ice production rate, 16.8 cm day⁻¹, for the month of May, (calculated using atmospheric
645 heat fluxes). Our median is also similar to Kurtz and Bromwich (1985), who also used a heat
646 budget to estimate an average ice production rate of 30 cm day⁻¹ for the month of May. All of
647 these estimates are smaller than the winter average from Sansiviero et al (2017) of 48.08 cm
648 day⁻¹ using a sea-ice model. Petrelli, Bindoff, & Bergamasco (2008) modeled a wintertime
649 maximum production rates of 26.4 cm day⁻¹ using a coupled atmospheric-sea ice model. Fusco et
650 al (2002) applied a model for latent heat polynyas and modeled production rate at 85 cm day⁻¹ for
651 1993 and 72 cm day⁻¹ for 1994.

652 The spatial trend we observed somewhat mimics the model 3D model of TNBP from
653 Gallee (1997) . During a four-day simulation, Gallee found highest ice production rates near the
654 coast (e.g. our Station 35) of 50 cm day⁻¹, and decreasing production to 0 cm day⁻¹ downstream
655 and at the outer boundaries, further west than PIPERS Station 33 (Figure 10). While some of the
656 ice production rates derived from PIPERS CTD profiles exceed prior results, we attribute that
657 excess to the relatively short time scale of these ice production “snapshots”. These estimates
658 integrate over minutes to tens of minutes, instead of days to months, therefore they are more
659 likely to capture the high frequency variability in this ephemeral process. As the katabatic winds
660 oscillate, the polynyas enter periods of slower ice production, driving average rates down.

661



662 Figure 10: TNBP map of ice production rates. Map of TNBP CTD stations with anomalies and
663 ice production rates. The CTD station number is listed in black and circled. Listed next to the
664 station is the respective ice production rate in cm day^{-1} . The production rates are colored by wind
665 speed: Green indicates wind speeds less than 10 m s^{-1} (Stations 28, 29, 33, 34, 35), Orange
666 indicates wind speeds between 10 and 15 m s^{-1} (Stations 25, 27, 30), and Red indicated wind
667 speeds over 15 m s^{-1} (Station 32).

668

669 **7. CONCLUSIONS**



670

671 Polynyas have been regarded as ice production factories with a wide range of modeled
672 production rates. During a late autumn oceanographic expedition to the Ross Sea, PIPERS
673 acquired CTD profiles in the ocean during strong katabatic wind events in both the Terra Nova
674 Bay polynya and the Ross Sea polynya. In those profiles we found near surface temperature and
675 salinity anomalies, which provided a new method for quantifying ice production rates in-situ.
676 Salinity and temperature anomalies observed at 11 CTD stations indicated frazil ice formation
677 and were used to estimate polynya ice production. Our estimated frazil ice production rates
678 varied from 7 to 378 cm day⁻¹. The wide range is likely capturing frazil ice production on very
679 short timescales (minutes). We note that the robustness of these estimates could be improved by
680 collecting consecutive CTD casts at the same location.

681 The polynyas in the Ross Sea show high ice production rates and are significant
682 contributors to Antarctic Bottom Water formation. Since 2015, sea ice extent around Antarctica
683 has decreased, with 2017 being an abnormally low year (Supplemental Figure 5; Fetterer et al,
684 2017). One of the goals of PIPERS was to understand if sea ice extent in the Ross Sea was
685 controlled primarily by ice production at the coast. If true, the decreased ice extent in recent
686 years may be related to changes in ice production in the polynyas. To further address these
687 questions, our estimates of polynya ice production can be paired with other ice products derived
688 from remote sensing, such as ice thickness from airborne and satellite lidar and ice area from
689 radar and passive microwave to better address the observed year-to-year changes. A decrease in
690 ice production rate correlates to freshening of Antarctic bottom water which would have global
691 impacts.

692

693

694

695

696

697

698



699 **8. REFERENCES**

700

701 Armstrong, T.: World meteorological organization: wmo sea-ice nomenclature. terminology,
702 codes and illustrated glossary, *J. Glaciol.*, 11, 148-149,

703 <https://doi.org.uri.idm.oclc.org/10.3189/S0022143000022577>, 1972.

704 Bromwich, D. H., and Kurtz, D. D.: Katabatic wind forcing of the terra nova bay polynya, *J.*
705 *Geophys. Res.*, 89, 3561-3572,

706 <https://doi.org.uri.idm.oclc.org/10.1029/JC089iC03p03561>, 1984.

707 Buffoni, G., Cappelletti, A., and Picco, P.: An investigation of thermohaline circulation in
708 terra nova bay polynya, *Antarct. Sci.*, 14.1, 83-92,
709 <https://doi.org.uri.idm.oclc.org/10.1017/S0954102002000615>, 2002.

710 Coachman, L. K.: Production of supercooled water during sea ice formation, *Proceedings of*
711 *the Symposium on Arctic Heat Budget and Atmospheric Circulation*, Lake Arrowhead,
712 California, 31 January–4 February 1966, 497–529, 1966.

713 Cosimo J.C., and Gordon A.L.: Inter-annual variability in summer sea ice minimum,
714 coastal polynyas and bottom water formation in the weddell sea, in: *Antarctic sea ice:*
715 *physical processes, interactions and variability*, 74, edited by: Jeffries, M.O., American
716 Geophysical Union, Washington, D.C., 293-315, <https://doi.org/10.1029/AR074p0293>,
717 1998.

718 Cox, G. F. N., and Weeks, W. F.: Equations for determining the gas and brine volumes in
719 sea-ice samples, *J. Glaciol.*, 29, 306-316, <https://doi.org/10.3189/S0022143000008364>,
720 1983.

721 Cushman-Rosin, B.: *Environmental Fluid Mechanics*, John Wiley & Sons, New York, 2019.

722 Dmitrenko, I. A., Wegner, C., Kassens, H., Kirillov, S. A., Krumpen, T., Heinemann, G.,
723 Helbig, A., Schroder, D., Holemann, J.A., Klagger, T., Tyshko, K.P., and Busche, T.:
724 Observations of supercooling and frazil ice formation in the laptev sea coastal polynya,
725 *J. Geophys. Res.*, 115, <https://doi.org.uri.idm.oclc.org/10.1029/2009JC005798>, 2010.

726 Fairall, C.W., Bradley, E.F., Hare, J.E., Grachev, A.A., and Edson, J.B.:
727 Bulk parameterization of air sea fluxes: updates and verification for the



728 COARE algorithm, *J. Climate*, 16, 571-590,
729 [https://doi.org/10.1175/1520-0442\(2003\)016<0571:BPOASF>2.0.CO;2](https://doi.org/10.1175/1520-0442(2003)016<0571:BPOASF>2.0.CO;2), 2003.

730 Fetterer, F., K. Knowles, W. N. Meier, M. Savoie, and A. K. Windnagel. 2017, updated
731 daily. *Sea Ice Index, Version 3*. Sea Ice Index, Version 3. Boulder, Colorado USA.

732 NSIDC: National Snow and Ice Data Center. <https://doi.org/10.7265/N5K072F8>. 09
733 March 2019.

734 Fusco, G., Flocco, D., Budillon, G., Spezie, G., and Zambianchi, E.: Dynamics and
735 variability of terra nova bay polynya, *Marine Ecology*, 23, 201–209,
736 <https://doi.org/10.1111/j.1439-0485.2002.tb00019.x>, 2002.

737 Fusco, G., Budillon, G., and Spezie, G.: Surface heat fluxes and thermohaline variability in
738 the ross sea and in terra nova bay polynya, *Cont. Shelf Res.*, 29(15), 1887-1895.
739 <https://doi.org/10.1016/j.csr.2009.07.006>, 2009.

740 Gallée, H.: Air-sea interactions over terra nova bay during winter: simulation with a
741 coupled atmosphere-polynya model, *J. Geophys. Res.-Atmos.*, 102, 13835–13849,
742 <https://doi.org/10.1029/96JD03098>, 1997.

743 Heorton, H. D. B. S., Radia, N., and Feltham, D. L.: A model of sea ice formation in leads
744 and polynyas, *J. Phys. Oceanogr.*, 47, 1701-1718,
745 <https://doi.org/10.1175/JPO-D-16-0224.1>, 2017.

746 Jacobs, S. S.: Bottom water production and its links with the thermohaline circulation,
747 *Antarct. Sci.*, 16, 427-437, <https://doi.org/10.1017/S095410200400224X>, 2004.

748 Jones, D. W. R. and Wells, A. J.: Frazil-ice growth rate and dynamics in mixed layers and
749 sub-ice-shelf plumes, *The Cryosphere*, 12, 25–38.
750 <https://doi.org/10.5194/tc-12-25-2018>, 2018.

751 Knuth, M. A. and Ackley, S. F.: Summer and early-fall sea-ice concentration in the ross
752 sea: comparison of in situ ASPeCt observations and satellite passive microwave
753 estimates, *Ann. Glaciol.*, 44, 303-309, <https://doi.org/10.3189/172756406781811466>,
754 2017.

755 Kurtz, D. D. and Bromwich, D. H.: A recurring, atmospherically forced polynya in terra
756 nova bay in *Antarctic Research Series*, 43, edited by: Jacobs, S.S., 43, American



757 Geophysical Union, Washington, D.C., 177-201, <https://doi.org/10.1029/AR043p0177>,
758 1985.

759 Lombardo, C., and Gregg, M.: Similarity scaling of viscous and thermal dissipation in a
760 convecting surface boundary layer., J. Geophys. Res., 94, , 6273-6284.
761 <https://doi.org/10.1029/JC094iC05p06273>, 1989.

762 Manwell, J. F., McGowan, J. G., and Rogers, A. L. Wind energy explained: theory, design
763 and application. John Wiley & Sons, West Sussex, England,
764 <https://doi.org/10.1002/9781119994367>, 2010.

765 Martin, S.: Frazil ice in rivers and oceans, Annu. Rev. Fluid Mech., 13(1), 379-397.
766 <https://doi.org/10.1146/annurev.fl.13.010181.002115>, 1981.

767 Martin, S., Drucker, R. S., and Kwok, R.: The areas and ice production of the western and
768 central ross sea polynyas, 1992-2002, and their relation to the B-15 and C-19 iceberg
769 events of 2000 and 2002, J. Marine Syst., 68, 201-214,
770 <https://doi.org/10.1016/j.jmarsys.2006.11.008>, 2007.

771 Mathiot, P., Jourdain, N., Barnier, C., Gallée, B., Molines, H., Sommer, J., and Penduff, M.:
772 Sensitivity of coastal polynyas and high-salinity shelf water production in the ross sea,
773 antarctica, to the atmospheric forcing, Ocean Dynam., 62(5), 701-723,
774 <https://doi.org/10.1007/s10236-012-0531-y>, 2012.

775 Matsumura, Y., and Ohshima, K. I.: Lagrangian modelling of frazil ice in the ocean, Ann.
776 Glaciol., 56(69),, 373-382, <https://doi.org/10.3189/2015AoG69A657>, 2017.

777 Michel, B.: Physics of snow and ice: morphology of frazil ice, International Conference on
778 Low Temperature Science. I, Conference on Physics of Snow and Ice, II, Conference
779 on Cryobiology, Sapporo, Japan, 14-19 August 1966, Sapporo, Japan, 119-128, 1967.

780 Monin, A. S., and Obukhov, A. M.: Basic laws of turbulent mixing in the surface layer of
781 the atmosphere, Contrib. Geophys. Inst. Acad. Sci. USSR, 24, 163-187, 1954.

782 Morales Maqueda, M. A., Willmott, A. J., and Biggs, N. R. T.: Polynya dynamics: a
783 review of observations and modeling, Rev. Geophys., 42(1), RG1004,
784 <https://doi.org/10.1029/2002RG000116>, 2004.



785 Orsi, A.H. and Wiederwohl, C.L.: A recount of ross sea waters, Deep-Sea Res. Pt. II,
786 56(13), 778-795, <https://doi.org/10.1016/j.dsr2.2008.10.033>, 2009.

787 Ozsoy-Cicek, B., Xie, H., Ackley, S. F., and Ye, K.: Antarctic summer sea ice concentration
788 and extent: comparison of ODEN 2006 ship observations, satellite passive microwave
789 and NIC sea ice charts, The Cryosphere, 3(1), 1-9, <https://doi.org/10.5194/tc-3-1-2009>,
790 2009.

791 Park, J., Kim, H.-C., Jo, Y.-H., Kidwell, A., and Hwang, J.: Multi-temporal variation of the
792 ross sea polynya in response to climate forcings, Polar Res., 37(1),
793 <https://doi.org/10.1080/17518369.2018.1444891>, 2018.

794 Pease, C. H.: The size of wind-driven coastal polynyas. J. Geophys. Res., 92(C7),
795 7049-7059, <https://doi.org/10.1029/JC092iC07p07049>, 1987.

796 Petrelli, P., Bindoff, N. L., and Bergamasco, A.: The sea ice dynamics of terra nova bay and
797 ross ice shelf polynyas during a spring and winter simulation, J. Geophys.
798 Res.-Oceans, 113(C9), <https://doi.org/10.1029/2006JC004048>, 2008.

799 Robinson, N. J., Williams, M. J., Stevens, C. L., Langhorne, P. J., and Haskell, T.
800 G.: Evolution of a supercooled ice shelf water plume with an actively growing subice
801 platelet matrix, J. Geophys. Res.-Oceans, 119(6), 3425-3446,
802 <https://doi.org/10.1002/2013JC009399>, 2014.

803 Sansiviero, M., Morales Maqueda, M. Á., Fusco, G., Aulicino, G., Flocco, D., and Budillon,
804 G.: Modelling sea ice formation in the terra nova bay polynya, J. Marine Syst., 166,
805 4-25, <https://doi.org/10.1016/j.jmarsys.2016.06.013>, 2017.

806 SBE 911plus CTD- SBE 911plus CTD Datasheet:
807 <https://www.seabird.com/profiling/sbe-911plus-ctd/family-downloads?productCategory=54627473769>, 15 August 2018, 2016.

808 Skogseth, R., Nilsen, F., and Smedsrud, L. H.: Supercooled water in an arctic polynya:
809 observations and modeling, J. Glaciol., 55(189), 43-52,
810 <https://doi.org/10.3189/002214309788608840>, 2009.



812 Smith, M., and Thomson, J.: Ocean surface turbulence in newly formed marginal ice zones,
813 J. Geophys. Res.-Oceans, 124(3), 1382-1398, <https://doi.org/10.1029/2018JC014405>,
814 2019.

815 Talley, L.D., Picard, G.L., Emery, W.J. Swift, J.H.: Descriptive physical oceanography: an
816 introduction, 6, Academic Press, Elsevier, Boston, 2011.

817 Tamura, T., Ohshima, K. I., and Nihashi, S.: Mapping of sea ice production for antarctic
818 coastal polynyas, Geophys. Res. Lett., 35(7), 1-5,
819 <https://doi.org/10.1029/2007GL032903>, 2008.

820 Thomson, J.: Wave breaking dissipation observed with “swift” drifters, J. Atmos. Ocean
821 Tech., 29(12), 1866–1882, <https://doi.org/10.1175/JTECH-D-12-00018.1>, 2012.

822 Thomson, J., Schwendeman, M., and Zippel, S. Wave-breaking turbulence in the ocean
823 surface layer., J. Phys. Oceanogr., 46, 1857–1870,
824 <https://doi.org/10.1175/JPO-D-15-0130.1>, 2016.

825 Ushio S., and Wakatsuchi, M.: A laboratory study on supercooling and frazil ice production
826 processes in winter coastal polynyas, J. Geophys. Res.-Oceans, 98(C11),
827 20321–20328, <https://doi.org/10.1029/93JC01905>, 1993.

828 Van Woert, M. L.: The wintertime expansion and contraction of the terra nova bay polynya,
829 Oceanography of the Ross Sea: Antarctica, Spezie, G. and Manzella, G. M. R.,
830 Springer, Milano, 145-164, https://doi.org/10.1007/978-88-470-2250-8_10, 1999a.

831 Van Woert, M. L.: Wintertime dynamics of the terra nova bay polynya, J. Geophys. Res.,
832 104, 7753-7769, <https://doi.org/10.1029/1999JC900003>, 1999b.

833 Weissling, B., Ackley, S., Wagner, P., and Xie, H.: EISCAM — Digital image acquisition
834 and processing for sea ice parameters from ships, Cold Reg. Sci. Technol., 57(1),
835 49-60, <https://doi.org/10.1016/j.coldregions.2009.01.001>, 2009.

836 Wilchinsky, A. V., Heorton, H. D. B. S., Feltham, D. L., and Holland, P. R.: Study of the
837 impact of ice formation in leads upon the sea ice pack mass balance using a new frazil
838 and grease ice parameterization, J. Phys. Oceanogr., 45(8), 2025–2047,
839 <https://doi.org/10.1175/JPO-D-14-0184.1>, 2015.



840 Worby, A. P., Geiger, C. A., Paget, M. J., Van Woert, M. L., Ackley, S. F., and DeLiberty, T.
841 L.: Thickness distribution of antarctic sea ice. *J. Geophys. Res. - Oceans*, 113(C5),
842 https://doi.org/10.1029/2007JC004254, 2008.

843 Zhang, G.: A further study on estimating surface evaporation using monthly mean data:
844 comparison of bulk formulations, *J. Climate*, 10(7), 1592-1600,
845 https://doi.org/10.1175/1520-0442(1997)010%3C1592:AFSOES%3E2.0.CO;2, 1997.

846 Zippel, S. F., and Thomson, J. (2016). Air-sea interactions in the marginal ice zone.
847 *Elementa Science of the Anthropocene*, 4, 95,
848 http://doi.org/10.12952/journal.elementa.000095, 2016.

849

850

851 8. ACKNOWLEDGEMENTS

852

853 The authors appreciate the support of the National Science Foundation through NSF Award Nos
854 1744562 (B. Loose, L. de Pace, URI); 134717 (S.F. Ackley, UTSA); 1341513 (E. Maksym,
855 WHOI); 1341725 (P. Guest, NPS); 1341606 (S. Stammerjohn and J. Cassano, U Colo). The
856 authors appreciate the support of the University of Wisconsin-Madison Automatic Weather
857 Station Program for the data set, data display, and information.

858

859 9. DATA AVAILABILITY

860

861 The data used in this publication are publicly available from the US Antarctic Program Data
862 Center <http://www.usap-dc.org/view/dataset/601192>

863

864 10. AUTHOR CONTRIBUTIONS

865

866 LD prepared the manuscript including all analysis. MS and JT provided SWIFT data and
867 guidance for upper ocean turbulence analysis. SS prepared and processed the PIPERS CTD data
868 and provided water mass insights during manuscript preparation; SA lead the PIPERS expedition



869 and supported ice interpretations. BL participated in PIPERS expedition, inferred possibility of
870 frazil ice growth and advised LD during manuscript preparation.

871

872 11. COMPETING INTERESTS

873

874 The authors declare that they have no conflict of interest."